

Multistate histogram-free reweighting for vapor-liquid coexistence calculations of non-simulated force field parameters

Richard A. Messerly,^{*,†} Mohammad S. Barhaghi,[‡] Jeffrey J. Potoff,[‡] and
Michael R. Shirts[¶]

[†]*Thermodynamics Research Center, National Institute of Standards and Technology, Boulder,
Colorado, 80305, United States*

[‡]*Department of Chemical Engineering and Materials Science, Wayne State University, Detroit,
Michigan 48202, United States*

[¶]*Department of Chemical and Biological Engineering, University of Colorado, Boulder,
Colorado, 80309, United States*

E-mail: richard.messerly@nist.gov

Contribution of NIST, an agency of the United States government; not subject to copyright in the United States.

Abstract

1 Introduction

A key advancement in molecular simulation is the ability to accurately and efficiently estimate vapor-liquid coexistence properties, i.e., saturated liquid density ($\rho_{\text{liq}}^{\text{sat}}$), saturated vapor density ($\rho_{\text{vap}}^{\text{sat}}$), saturated vapor pressures ($P_{\text{vap}}^{\text{sat}}$), and enthalpy of vaporization (ΔH_v). The accuracy of coexistence estimates depends on the underlying molecular model (a.k.a., force field, potential model, or Hamiltonian) while the computational efficiency depends primarily on the simulation methods. Due to the abundance of experimental vapor-liquid coexistence data and the sensitivity of such properties to both short- and long-range non-bonded interactions, numerous force fields have been parameterized using $\rho_{\text{liq}}^{\text{sat}}$, $P_{\text{vap}}^{\text{sat}}$, and ΔH_v . Although the development of accurate force fields has been greatly enabled by the improved efficiency of simulation methods, parameterization of non-bonded interactions with vapor-liquid coexistence calculations remains an arduous and time-consuming task.¹⁻³

Several methods exist for computing vapor-liquid coexistence properties, e.g., Gibbs Ensemble Monte Carlo (GEMC), two phase molecular dynamics (2 ϕ MD), isothermal-isochoric integration (ITIC), and Grand Canonical Monte Carlo coupled with histogram reweighting (GCMC-HR). Advantages and disadvantages exist for each method. For example, GEMC and GCMC require insertion moves that are computationally inefficient for complex molecular structures with high density liquid phases. Several advanced simulation techniques are available to overcome this challenge,⁴ which has enabled GEMC and GCMC-HR to be the primary methods of choice for vapor-liquid coexistence calculations.

Some clear advantages and disadvantages exist for GCMC-HR compared with GEMC. For example, one advantage of GCMC-HR is the higher precision.⁵ Furthermore, coexis-

tence properties can be computed at temperatures that are not simulated directly. However, GEMC is arguably more straightforward in that simulations are performed only at the desired saturation temperatures (T^{sat}). By contrast, GCMC-HR requires a series of GCMC simulations for a single T^{sat} . This set includes a near-critical simulation that “bridges” the vapor and liquid phases. Obtaining the appropriate chemical potential (μ) for this bridge simulation is a cumbersome and, typically, iterative process (although more advanced methods exist to obtain a good initial estimate for μ ⁶).

Another disadvantage of GCMC-HR compared to GEMC is that GCMC-HR requires more post-processing (i.e., histogram reweighting), while simple block averaging is typically sufficient for GEMC. Histogram reweighting (and more generally, configuration reweighting) is an important tool in many fields of molecular simulation. In fact, it has long since been known that it is possible to estimate properties for state “j” by reweighting configurations that were sampled with state “i.”^{7–10} For example, umbrella sampling simulations are often processed using the weighted histogram analysis method (WHAM) to compute free energy differences between states. A popular alternative to WHAM is the Multistate Bennett Acceptance Ratio (MBAR),^{11,12} which is readily available in the *pymbar* package.

In this study, we substitute HR with MBAR for the GCMC-HR approach of computing vapor-liquid coexistence properties. Section 2.3 demonstrates that MBAR and HR are mathematically equivalent (in the limit of zero bin width) while Section 3 shows that they are also numerically equivalent (to within statistical uncertainties). Note that, as Boulougouris et al. demonstrate how to combine HR with GEMC (GEMC-HR) to estimate saturation properties at non-simulated temperatures,¹³ MBAR could alternatively be applied to GEMC simulations.

Substituting the standard HR approach with MBAR is not the primary purpose of this study. Rather, we demonstrate how GCMC-MBAR can also estimate coexistence proper-

ties for non-simulated parameter sets, which can greatly accelerate force field parameterization. In a similar study, Messerly et al. demonstrate how to combine MBAR with ITIC (MBAR-ITIC) to optimize Mie λ -6 (generalized Lennard-Jones) potentials.^{14,15} For MBAR-ITIC, a series of NVT simulations along an isotherm and isochores are performed with a “reference” force field (θ_{ref}). MBAR computes the internal energy (U) and pressure (P) (or compressibility factor, Z) for each $T - \rho$ state point with a non-simulated (“rerun”) force field (θ_{rr}). ITIC then converts the U and P values into vapor-liquid coexistence properties.^{16,17}

The results from Messerly et al. demonstrate that MBAR-ITIC is most reliable in the local domain, i.e., for parameter sets near the “reference” parameter set from which configurations are sampled.¹⁴ Furthermore, MBAR-ITIC performs best for changes in the non-bonded well-depth parameter (ϵ) while it performs significantly worse for large changes in the non-bonded size and repulsive parameters (σ and λ , respectively). This is typically referred to as poor “overlap” and can be quantified by the “number of effective samples” (N_{eff}). Poor overlap (low N_{eff}) is especially problematic for ITIC as a large number of snapshots is needed to obtain precise estimates of P in the liquid phase, which are essential to obtain reasonable values of $\rho_{\text{liq}}^{\text{sat}}$.

Our hypothesis is that GCMC-MBAR should have better overlap over the non-bonded parameter space than what was observed for MBAR-ITIC. There are two main reasons for this hypothesis/aspiration. First, the fluctuating densities of GCMC simulations, as opposed to the fixed density NVT simulations, accommodate a wider range of configurations and energies. Second, ITIC requires accurate calculations of U and P in the vapor phase, which necessitate larger box sizes (and, thereby, more molecules) than those typically utilized with GCMC. By utilizing fewer molecules, GCMC simulations experience larger energy fluctuations (on a percent basis) which improves the overlap between states. We also hypothesize that the impact of poor overlap is less severe compared to

ITIC, where poor overlap leads to sporadic coexistence estimates.

Note that the method outlined in this study is similar in spirit to “Hamiltonian scaling” (HS), which has been applied to both GEMC and GCMC simulations. The HS approach samples from multiple force fields (Hamiltonians) in a single simulation according to a weighted sampling probability. Vapor-liquid coexistence curves for each force field are estimated post-simulation by reweighting the configurations accordingly. For the Grand Canonical Monte Carlo implementation of Hamiltonian scaling (HS-GCMC), μ and T are not stationary during the simulation, rather the current value of μ and T depends on which force field is being sampled. Despite HS-GCMC proving to be a powerful tool to optimize force field parameters,^{10,18–20} it has yet to gain widespread popularity. This is likely due to the added complexity of both the simulation protocol and the histogram post-processing. Also, HS requires that a decision be made *a priori* regarding which force fields are to be tested. By contrast, MBAR does not require any modification of the simulation procedure, the post-processing is essentially unchanged, and the non-bonded parameter sets need not be selected prior to the simulations.

Recently, Weidler and Gross proposed “individualized,” i.e., compound-specific, parameter sets for compounds which contain large amounts of experimental data.²¹ To avoid overfitting, a one-dimensional optimization is employed which scales ϵ for all united-atom sites while not adjusting σ or λ . MBAR is ideally suited for this “ ϵ -scaling” approach for at least two reasons. First, as mentioned previously, MBAR is most reliable when extrapolating in ϵ rather than σ and/or λ . Second, the rate-limiting step for MBAR is recomputing the configurational energies for a different force field. Furthermore, storing millions of configuration “snapshots” is highly memory intensive. While basis functions (see Section 2.4) alleviate the additional computational cost and reduce the memory load, ϵ -scaling does not require storing/recomputing configurations or basis functions. Instead, the energies for each snapshot are simply multiplied by the ϵ -scaling parameter.

The outline for this study is the following. Section 2 provides details regarding the force fields, simulation set-up, and post-simulation analysis with MBAR. Section 3 provides a comparison of GCMC-MBAR and GCMC-HR as well as various applications of GCMC-MBAR for force field parameterization. Section 4 discusses some limitations and provides recommendations for future work. Section 5 presents the primary conclusions.

2 Methods

2.1 Force fields

The force fields utilized in this study are Transferable Potentials for Phase Equilibria (TraPPE-UA, also referred to simply as TraPPE^{1,22,23}), Potoff,^{3,24} and Nath, Escobedo, and de Pablo revised (NERD). Each force field adopts a united-atom (UA) representation, where non-polar hydrogens are not modeled explicitly. The non-bonded potential is of the generalized Lennard-Jones (Mie λ -6) form.

The bond lengths for the TraPPE, Potoff, and NERD force fields are 0.154 nm for all compounds studied. The same angle and dihedral potentials are used for each force field. Angular bending interactions are evaluated using a harmonic potential:

$$u^{\text{bend}} = \frac{k_{\theta}}{2} (\theta - \theta_0)^2 \quad (1)$$

where u^{bend} is the bending energy, θ is the instantaneous bond angle, θ_0 is the equilibrium bond angle (see Table 1), and k_{θ} is the harmonic force constant with $k_{\theta}/k_{\text{B}} = 62500 \text{ K/rad}^2$ for all bonding angles, where k_{B} is the Boltzmann constant.

Dihedral torsional interactions are determined using a cosine series:

$$u^{\text{tors}} = c_0 + c_1[1 + \cos \phi] + c_2[1 - \cos 2\phi] + c_3[1 + \cos 3\phi] \quad (2)$$

Table 1: Equilibrium bond angles (θ_0).²² CH_i and CH_j represent CH_3 , CH_2 , CH , or C sites.

Bending sites	θ_0 (degrees)
$\text{CH}_i\text{-CH}_2\text{-CH}_j$	114.0
$\text{CH}_i\text{-CH-CH}_j$	112.0
$\text{CH}_i\text{-C-CH}_j$	109.5

where u^{tors} is the torsional energy, ϕ is the dihedral angle and c_n are the Fourier constants listed in Table 2.

Table 2: Fourier constants (c_n/k_B) in units of K.²² CH_i and CH_j represent CH_3 , CH_2 , CH , or C sites.

Torsion sites	c_0/k_B	c_1/k_B	c_2/k_B	c_3/k_B
$\text{CH}_i\text{-CH}_2\text{-CH}_2\text{-CH}_j$	0.0	355.03	-68.19	791.32
$\text{CH}_i\text{-CH}_2\text{-CH-CH}_j$	-251.06	428.73	-111.85	441.27
$\text{CH}_i\text{-CH}_2\text{-C-CH}_j$	0.0	0.0	0.0	461.29
$\text{CH}_i\text{-CH-CH-CH}_j$	-251.06	428.73	-111.85	441.27

Non-bonded interactions between sites located in two different molecules or separated by more than three bonds within the same molecule are calculated using a Mie λ -6 potential (of which the Lennard-Jones, LJ, 12-6 is a subclass):

$$u^{\text{nb}}(\epsilon, \sigma, \lambda; r) = \left(\frac{\lambda}{\lambda - 6} \right) \left(\frac{\lambda}{6} \right)^{\frac{6}{\lambda - 6}} \epsilon \left[\left(\frac{\sigma}{r} \right)^\lambda - \left(\frac{\sigma}{r} \right)^6 \right] \quad (3)$$

where u^{nb} is the van der Waals interaction, σ is the distance (r) where $u^{\text{nb}} = 0$, $-\epsilon$ is the energy of the potential at the minimum (i.e., $u^{\text{nb}} = -\epsilon$ and $\frac{\partial u^{\text{nb}}}{\partial r} = 0$ for $r = r_{\text{min}}$), and λ is the repulsive exponent.

The non-bonded Mie λ -6 force field parameters for TraPPE, Potoff, and NERD are provided in Table 3. Potoff reports a “generalized” and “short/long” (S/L) CH and C parameter set. The “short” and “long” parameters are implemented when the number of

carbons in the backbone is ≤ 4 and > 4 , respectively. Also note that the NERD force field has several different parameter sets for CH_3 sites.

Table 3: Non-bonded (intermolecular) parameters for TraPPE,^{1,22} Potoff,^{3,24} and NERD.²⁵

United-atom	ϵ/k_B (K)	σ (nm)	λ
TraPPE			
CH_3	98 (134.5)	0.375 (0.352)	12
CH_2	46	0.395	12
CH	10	0.468	12
C	0.5	0.640	12
Potoff			
CH_3	121.25	0.3783	16
CH_2	61	0.399	16
CH, gen.	15	0.46	16
C, gen.	1.2	0.61	16
CH, short	15	0.47	16
C, short	1.45	0.61	16
CH, long	14	0.47	16
C, long	1.2	0.62	16
NERD			
CH_3	104.00	0.3910	12
CH_3 (2-methylpropane)	78.23	0.3880	12
CH_3 (2,2-dimethylpropane)	74.50	0.3910	12
CH_2	45.80	0.3930	12
CH	39.70	0.3850	12
C	17.00	0.3910	12

Non-bonded parameters between two different site types (i.e., cross-interactions) are determined using Lorentz-Berthelot combining rules²⁶ for ϵ and σ and an arithmetic mean for the repulsive exponent λ (as recommended in Reference 3):

$$\epsilon_{ij} = \sqrt{\epsilon_{ii}\epsilon_{jj}} \quad (4)$$

$$\sigma_{ij} = \frac{\sigma_{ii} + \sigma_{jj}}{2} \quad (5)$$

$$\lambda_{ij} = \frac{\lambda_{ii} + \lambda_{jj}}{2} \quad (6)$$

where the ij subscript refers to cross-interactions and the subscripts ii and jj refer to same-site interactions.

2.2 Simulation set-up

The majority of results presented in Section 3 are obtained by reprocessing simulation output that were analyzed in previous studies utilizing histogram reweighting.^{24,27} New simulation results are provided for *n*-hexane, 2-methylpropane, 2,2-dimethylpropane, 2,2,4-trimethylhexane, 2,3-dimethylbutane, 2,3,4-trimethylpentane, 2,2,3,3-tetramethylbutane, and cyclohexane. All simulations are performed using GPU optimized Monte Carlo (GOMC) with Grand Canonical Monte Carlo (GCMC), where the chemical potential (μ), volume (V), and temperature (T) are constant.

A series of nine simulations are performed, two in the vapor phase, six in the liquid phase, and one near critical which acts as the “bridge” between the vapor and liquid phases. A low-density (less than twenty molecules) initial configuration is utilized for the vapor phase simulations, while the bridge and liquid phase simulations are initialized with a high-density (around 200 molecules) configuration. The system volume is the same for each simulation, but varies somewhat between compounds. The prescribed chemical potentials and temperatures for the branched alkanes are the same as those utilized in Mick et al.²⁴ The $\mu - T$ values for *n*-hexane and cyclohexane are determined in this study. All state points are reported in Supporting Information.

The equilibration stage for each GCMC simulation consists of 2×10^7 Monte Carlo steps (MCS). The production stage is 4×10^7 MCS for vapor simulations and 2.5×10^7 MCS for the liquid and “bridge” simulations. Snapshots (i.e., number of molecules, internal energy, and optionally the xyz coordinates) are stored every 200 MCS to reduce

the correlation between sequential configurations. Thus, the total number of snapshots (N_{snaps}) is 2×10^5 for vapor simulations and 1.25×10^5 for liquid and “bridge” simulations. The type of Monte Carlo move implemented for each step is selected randomly with a 20%, 10%, and 70% probability of performing a displacement, rotation, and particle swap move, respectively. The move probabilities are slightly different for cyclohexane, namely, 30%, 10%, 40%, and 20% for displacement, rotation, particle swap, and crank-shaft moves, respectively.

Four different applications for MBAR are demonstrated in this study, where slightly different types of simulation output are required. First, we demonstrate how MBAR yields consistent results to those previously reported using histogram reweighting. The standard simulation output is used in this application, namely, a $2 \times N_{\text{snaps}}$ array containing the number of molecules and the internal energy for all N_{snaps} snapshots. Second, we demonstrate how these same data can be used with MBAR to predict VLE properties when performing ϵ -scaling. Third, we investigate how well MBAR can predict VLE for force field “j” from sampled states of force field “i.” In this case, a $3 \times N_{\text{snaps}}$ array is required, where the additional column is the internal energy computed with force field “j” for the configurations sampled with force field “i.” Fourth, we demonstrate how storing basis functions is a computationally efficient method for predicting VLE for multiple force fields that are unknown at runtime.

2.3 Multistate Bennett Acceptance Ratio

The GCMC approach for estimating phase coexistence requires significant post-processing. Before demonstrating how we implement MBAR for this purpose, we review the traditional histogram reweighting approach. We also discuss the steps of this procedure that are the same for both HR and MBAR. We refer the interested reader to the literature for derivations and more detailed discussion of the GCMC-HR equations (cf. 10).

MRSHIRTS: I would like the MBAR and histogram reweighting equations to be consistent with each other in the limit of zero bin-width and a single reference force field. Here is how HR is presented in the literature, verbatim:

The probability of observing N particles with internal energy U for a given chemical potential (μ) and inverse temperature ($\beta \equiv \frac{1}{k_B T}$ where k_B is the Boltzmann constant) is

$$p(N, E; \mu, \beta) = \frac{\sum_{i=1}^R f_i(N, E) \exp(-\beta E + \beta \mu N)}{\sum_{i=1}^R K_i \exp(-\beta_i U + \beta_i \mu_i N - C_i)} \quad (7)$$

where $f_i(N, E)$ is the probability of occurrence N particles in the simulation cell with total configurational energy in the vicinity of E , K_i is the total number of observations ($K_i = \sum_{N,E} f_i(N, E)$) for run i . The constants C_i (also known as “weights”) are obtained by iteration from the relationship

$$\exp(C_i) = \sum_E \sum_N p(N, E; \mu_i, \beta_i) \quad (8)$$

Given an initial guess for the set of weights C_i , Equations 7 and 8 can be iterated until convergence. The ensemble average for a given observable is

$$\langle O \rangle_{\mu, \beta} = \sum_E \sum_N p(N, E; \mu, \beta) \times O \quad (9)$$

The pressure of a system can be obtained from the following expression. If the conditions for run 1 are (μ_1, V, β_1) and for run 2 (μ_2, V, β_2) , then

$$C_2 - C_1 = \ln \frac{\Xi(\mu_2, V, \beta_2)}{\Xi(\mu_1, V, \beta_1)} = \beta_2 P_2 V - \beta_1 P_1 V \quad (10)$$

where P is the pressure, since $\ln \Xi = \beta P V$. Equation 10 can be used to obtain the absolute value of the pressure for one of the two runs, provided that the absolute pressure can be

estimated for the other run. Typically, this is done by performing simulations for low-density states for which the system follows the ideal gas equation of state, $PV = Nk_B T$.

MRSHIRTS: Here is how I reported the MBAR equations in our first publication:

With MBAR the expectation $\langle O(\theta) \rangle$ for force field (θ) of any given observable (O) can be expressed as:

$$\langle O(\theta) \rangle = \sum_{n=1}^N O(\mathbf{x}_n; \theta) W_n(\theta) \quad (11)$$

where \mathbf{x}_n are configurations sampled from one or more reference force fields (θ_{ref}), $O(\mathbf{x}_n; \theta)$ is the observable value using force field θ with configurations \mathbf{x}_n , and $W_n(\theta)$ is the weight of the n^{th} configuration using force field θ , calculated by using:

$$W_n(\theta) = \frac{\exp[\hat{f}(\theta) - u(\mathbf{x}_n; \theta)]}{\sum_{k=1}^K N_k \exp[\hat{f}(\theta_{\text{ref},k}) - u(\mathbf{x}_n; \theta_{\text{ref},k})]} \quad (12)$$

where the reduced free energies ($\hat{f}(\theta)$) are calculated with:

$$\hat{f}(\theta) = -\ln \sum_{n=1}^{N_{\text{snaps}}^{\text{tot}}} \frac{\exp[-u(\mathbf{x}_n; \theta)]}{\sum_{k=1}^K N_k \exp[\hat{f}(\theta_{\text{ref},k}) - u(\mathbf{x}_n; \theta_{\text{ref},k})]} \quad (13)$$

where K is the number of reference force fields, $N_{\text{snaps}}^{\text{tot}} = \sum_k N_k$ is the total number of snapshots for all K reference force fields, N_k are the total number of snapshots from the k^{th} reference force field, $\theta_{\text{ref},k}$ is the k^{th} reference (i.e. simulated) force field, and $u(\mathbf{x}_n; \theta)$ is the reduced potential energy evaluated with θ for configuration \mathbf{x}_n . For the grand canonical ensemble, $u(\mathbf{x}_n; \theta) = \beta U(\mathbf{x}_n; \theta) - \beta \mu N$, where $\beta = \frac{1}{k_B T}$ and k_B is the Boltzmann constant.

Note that $\hat{f}(\theta_{\text{ref},k})$ is required to evaluate the denominator of Equations 12-13. The

values for $\hat{f}(\theta_{\text{ref},k})$ are obtained by solving a system of K equations for self-consistency. Specifically, an initial guess for $\hat{f}(\theta_{\text{ref},k})$ is used to evaluate Equation 13 with $\theta = \theta_{\text{ref},k}$ to obtain updated values of $\hat{f}(\theta_{\text{ref},k})$. This process is repeated until the values for $\hat{f}(\theta_{\text{ref},k})$ converge to within a desired tolerance. Although solving the MBAR system of equations for self-consistency may require several iterations, fortunately, once this process has been performed $\hat{f}(\theta)$ (for an arbitrary θ) is evaluated without further iteration.

The performance of MBAR depends strongly on good phase space overlap, meaning that the configurations sampled by the reference force field(s) must represent a significant portion of the “true” configurations that the non-simulated force field would sample.²⁸ If the configurational overlap is small the MBAR estimates are likely dominated by a few configurations, which are likely not representative of the ensemble that would be generated by direct simulation of force field θ . The amount of overlap can be quantified by the number of effective samples (N_{eff}),²⁹ using Kish’s formula:

$$N_{\text{eff}} = \frac{(\sum_n W_n)^2}{\sum_n W_n^2} \quad (14)$$

which reduces to $N_{\text{eff}} = (\sum_n W_n^2)^{-1}$ when the weights are normalized. This has the property that when the weights are equal, $N_{\text{eff}} = N$, when all but one weight is negligible, $N_{\text{eff}} \approx 1$, and behaves appropriately for intermediate cases. In the case of poor overlap ($N_{\text{eff}} \approx 1$), the predicted values of MBAR will demonstrate a strong bias and the uncertainties will likely be underestimated by the MBAR covariance matrix.

1. Traditionally, histogram reweighting (HR) has been applied with GCMC to calculate vapor-liquid coexistence properties
2. Present histogram reweighting equations
3. Discuss how to compute phase equilibria by equating pressures

4. Discuss how to compute heat of vaporization
5. In this study, we demonstrate how to compute VLE using MBAR-GCMC
6. Procedure is identical to that utilized for HR but using the MBAR equations
7. Present MBAR equations
8. MBAR for $\theta = \theta_{\text{ref}}$ is mathematically equivalent to histogram reweighting in the limit of zero bin width
9. MBAR-GCMC allows for prediction of multiple force fields from single simulation without modifying force fields mid-simulation (i.e., Hamiltonian scaling approach)
10. MBAR uncertainties are computed using bootstrap resampling

2.4 Basis functions

1. When applying MBAR to different parameter sets, $\theta \neq \theta_{\text{ref}}$, it is necessary to recompute energies
2. Basis functions accelerate the recompute energy step by storing the repulsive and attractive contributions that can be scaled by ϵ and σ
3. Basis functions are computed from GOMC using the recompute feature for different ϵ and σ and solving system of equations

3 Results

This section presents results from several different applications of GCMC-MBAR. First, we compute vapor-liquid coexistence properties in the case where the force field parameters do not change, i.e., $\theta_{\text{rr}} = \theta_{\text{ref}}$. Second, we perform a one-dimensional optimization

in the ϵ -scaling parameter, ψ . This requires applying GCMC-MBAR with $\epsilon_{\text{rr}} = \psi \times \epsilon_{\text{ref}}$ while $\sigma_{\text{rr}} = \sigma_{\text{ref}}$ and $\lambda_{\text{rr}} = \lambda_{\text{ref}}$. Third, we determine the reliability of GCMC-MBAR when $\theta_{\text{rr}} \neq \theta_{\text{ref}}$ for different literature force fields. Fourth, we demonstrate how GCMC-MBAR can be applied to obtain new Mie λ -6 parameters for cyclohexane.

Section 2.3 demonstrated that MBAR and HR are mathematically equivalent in the limit of zero bin width and when $\theta_{\text{rr}} = \theta_{\text{ref}}$. Figure 1 provides numerical validation that GCMC-MBAR and GCMC-HR yield indistinguishable vapor-liquid coexistence properties. Note that the median percent deviation is approximately zero and that the largest deviations are within a few percent. The percent deviations shown in Figure 1 are averaged over the 31 branched alkanes studied by Mick et al. and the 11 alkynes studied by Barhaghi et al. The GCMC-HR values were not recomputed in this study but were taken from the literature.^{24,27} The GCMC-MBAR values were computed using the same raw simulation data as Mick et al. and Barhaghi et al. The only difference being that a single replicate was used to compute GCMC-MBAR values, whereas GCMC-HR used data from all five replicates.

Reference 21 proposed an ϵ -scaling approach for converting transferable parameters (TAMie) into compound-specific or individualized parameters (iTAMie). The philosophy being individualized parameters is that some compounds have sufficient reliable experimental data that a force field can be refined to improve the agreement. Refitting all non-bonded parameters simultaneously could lead to an overfit parameter set, which would likely perform poorly at state points outside of the training set. For this reason, Weidler et al. optimize a single adjustable parameter (ψ) that scales all the ϵ values according to

$$\epsilon_{ii}^{\text{ind}} = \psi \epsilon_{ii}^{\text{tran}} \quad (15)$$

where $\epsilon_{ii}^{\text{ind}}$ is the individualized ϵ value for united-atom ii and $\epsilon_{ii}^{\text{tran}}$ is the corresponding

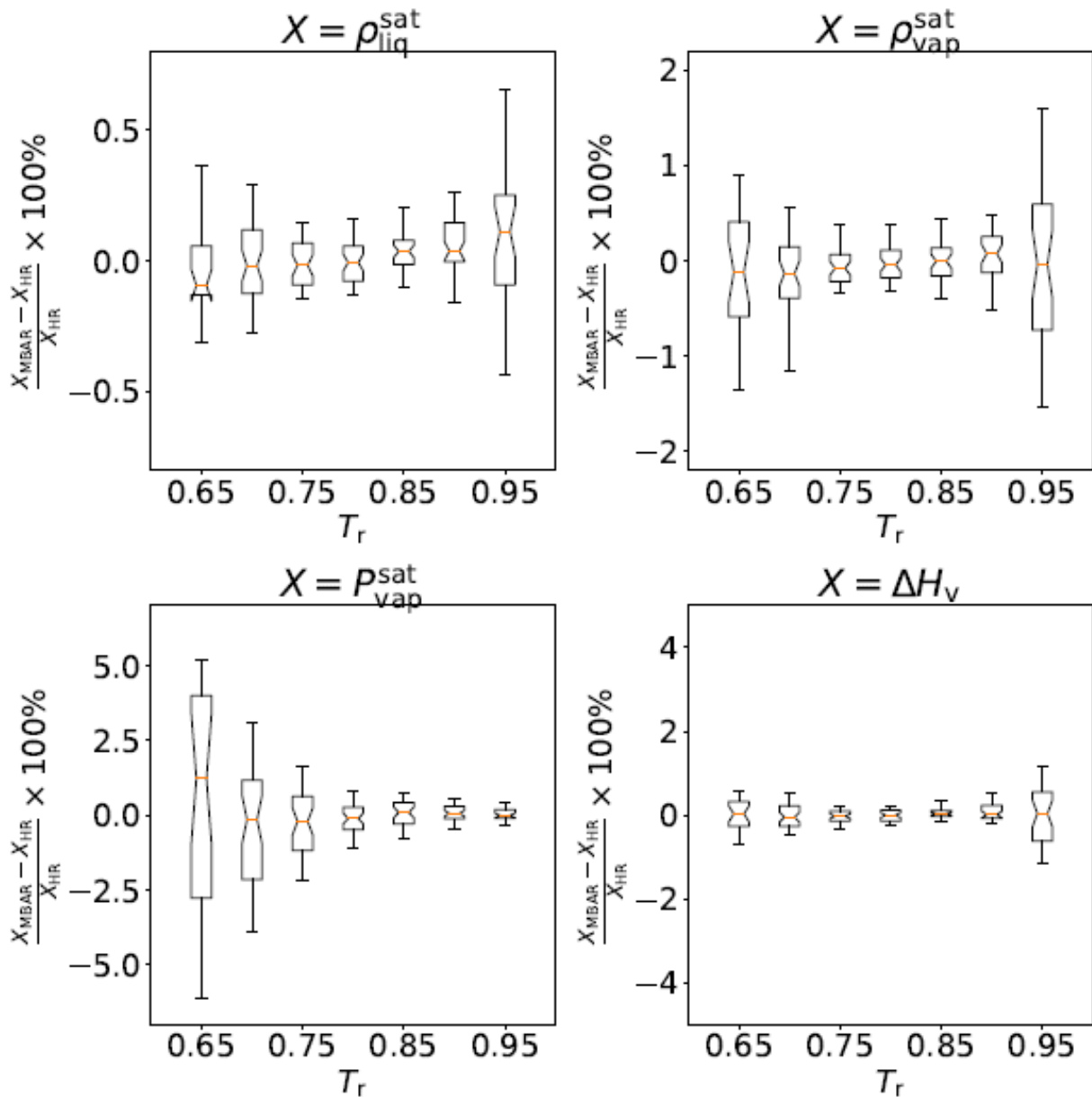


Figure 1: Percent deviations between coexistence properties computed using histogram reweighting (HR) and Multistate Bennett Acceptance Ratio (MBAR). Top-left, top-right, bottom-left, and bottom-right panels correspond to saturated liquid density, saturated vapor density, saturated vapor pressure, and enthalpy of vaporization, respectively. Boxes depict the first and third quartiles while whiskers represent the range that contains 95% of the data.

transferable ϵ value. A truly transferable force field should have $\psi \approx 1$ for all compounds.

Weigler et al. tend to characterize the individualization as being useful when the scaling

is greater than 0.4% (i.e., $|1 - \psi| > 0.004$).

Figure 2 shows that the alkynes require a greater degree of scaling than the branched alkanes. The TAMie force field also found $\psi \approx 1$ for branched alkanes. Although ψ values for iTAMie were not reported for alkynes, the largest ψ value for olefins, ethers, and ketones was ≈ 1.01 . Therefore, the transferability of the Potoff force field appears to be slightly poorer for 2-pentyne and 2-hexyne, which have an optimized $\psi > 1.01$. It is also interesting that only 3 out of 19 compounds require $\psi < 1$. By contrast, this trend was not observed in Reference 21.

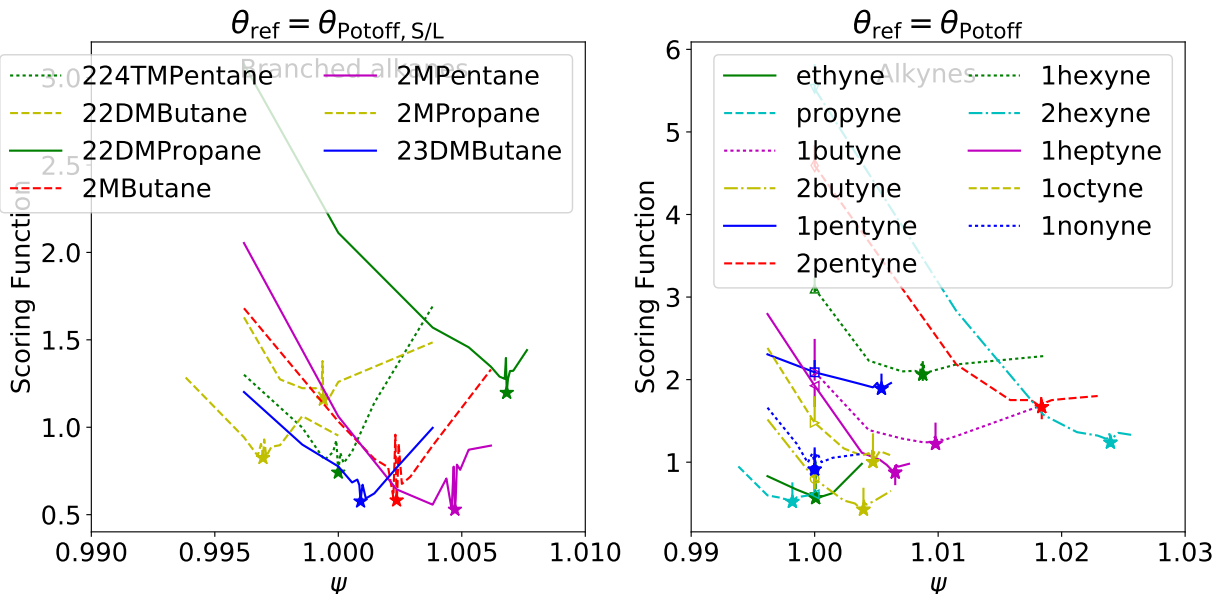


Figure 2: One dimensional optimization with ϵ -scaling (ϕ) of Potoff-SL for select branched alkanes (left) and alkynes (right). Open symbols correspond to the original force field, i.e., $\phi = 1$, while the filled stars are the optimal ϕ value for a given compound.

At least two reasons exist for why MBAR is ideally suited for ϵ -scaling. First, the energies in Equation ?? can be scaled by ϕ such that the configurations do not need to be stored or recomputed. Second, MBAR is more reliable for changes in ϵ rather than changes in σ and/or λ .¹⁴ A more demanding test of GCMC-MBAR is to vary several parameters simultaneously, including σ and λ . Because it is not possible to visualize a

parameter space of greater than two dimensions, we perform this analysis of GCMC-MBAR using the TraPPE, NERD, Potoff-gen, and Potoff-SL force fields. Specifically, we use GCMC-MBAR to predict coexistence properties of the TraPPE force field by sampling configurations with Potoff-gen, and vice versa (see Figure 4). We also predict coexistence properties for the NERD and Potoff-SL force fields using configurations sampled from TraPPE and Potoff-gen, respectively (see Figure 3).

Note that all three non-bonded parameters (ϵ , σ , and λ) for all four united-atom types (CH_3 , CH_2 , CH , and C) are different between the TraPPE and Potoff-gen force fields. The TraPPE and NERD ϵ and σ values are different for all four united-atom types while $\lambda = 12$ for both force fields. The Potoff-gen and Potoff-SL force fields only differ in the ϵ and/or σ values for the CH and C sites. Specifically, the 2-methylpropane parameters are identical except for σ_{CH} , the 2,2-dimethylpropane parameters are the same except for ϵ_{C} , and three parameters are different for 2,2,4-trimethylpentane (ϵ_{CH} , σ_{CH} , and σ_{C}). However, the difference in ϵ and σ values for Potoff-gen and Potoff-SL is significantly smaller than that between TraPPE and NERD.

Figures 3 and 4 compare the GCMC-MBAR predicted values for $\theta_{\text{rr}} \neq \theta_{\text{ref}}$ to those for $\theta_{\text{rr}} = \theta_{\text{ref}}$. Figure 3 contains $\lambda_{\text{rmrr}} = \lambda_{\text{ref}}$ while Figure 4 corresponds to $\lambda_{\text{rmrr}} \neq \lambda_{\text{ref}}$. Overall, MBAR is extremely reliable at predicting vapor phase properties ($\rho_{\text{vap}}^{\text{sat}}$ and $P_{\text{vap}}^{\text{sat}}$) while it is less reliable for liquid phase properties ($\rho_{\text{liq}}^{\text{sat}}$ and ΔH_{v} , which depends on both phases). In particular, note that the $\rho_{\text{liq}}^{\text{sat}}$ estimates in Figure 4 are sporadic and unreliable. This can be explained by the low number of effective samples in the liquid phase, which demonstrate that the repulsive exponent (λ) greatly impacts the configurational overlap in the liquid phase.

1. We validate that MBAR and HR are indistinguishable by re-analyzing the simulation results of Mick et al. and Barhaghi et al. utilizing MBAR

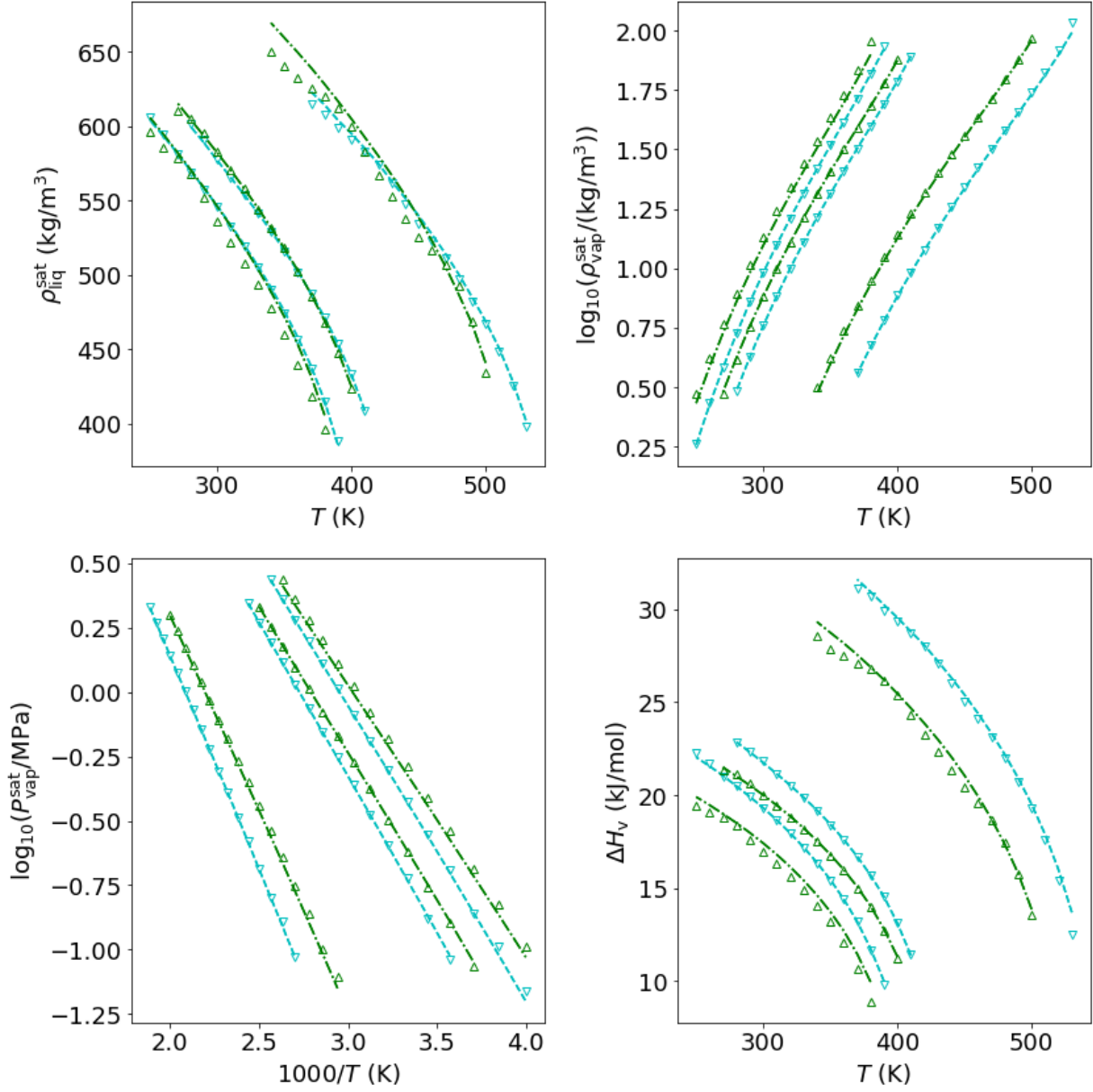


Figure 3: Comparison between MBAR-GCMC estimates (symbols) for $\theta_{rr} \neq \theta_{ref}$ and literature (MBAR-HR) values (lines) for $\theta_{rr} = \theta_{ref}$ with a constant repulsive exponent, i.e., $\lambda_{rr} = \lambda_{ref}$. MBAR-GCMC estimates for the NERD and Potoff-SL force fields are computed using configurations sampled from TraPPE and Potoff-gen, respectively. Top-left, top-right, bottom-left, and bottom-right panels correspond to saturated liquid density, saturated vapor density, saturated vapor pressure, and enthalpy of vaporization, respectively.

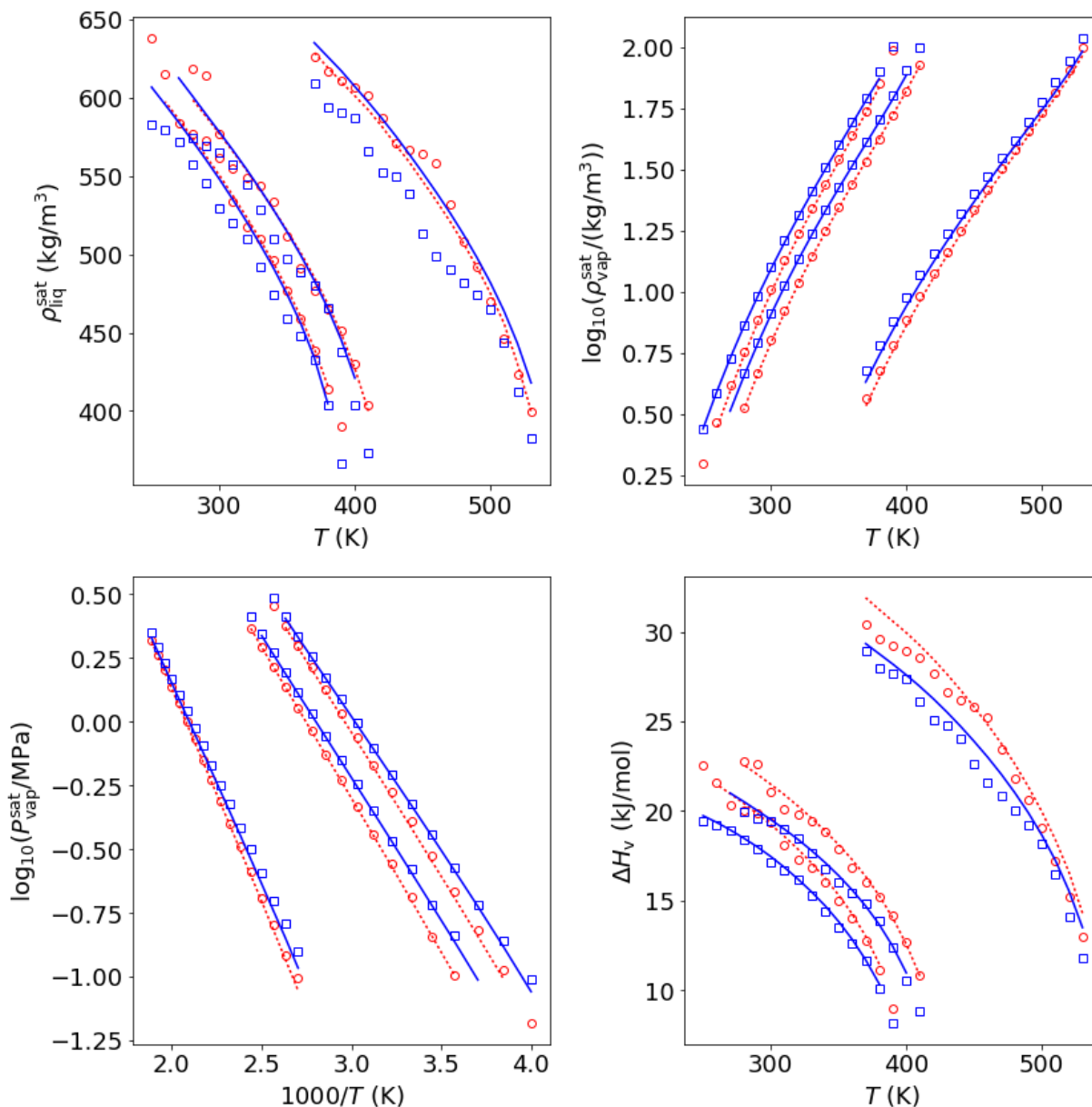


Figure 4: Comparison between MBAR-GCMC estimates (symbols) for $\theta_{rr} \neq \theta_{ref}$ and literature (MBAR-HR) values (lines) for $\theta_{rr} = \theta_{ref}$ with a non-constant repulsive exponent, i.e., $\lambda_{rr} \neq \lambda_{ref}$. MBAR-GCMC estimates for the TraPPE force field are computed using configurations sampled from Potoff-gen, and vice versa. Top-left, top-right, bottom-left, and bottom-right panels correspond to saturated liquid density, saturated vapor density, saturated vapor pressure, and enthalpy of vaporization, respectively.

2. Epsilon scaling for all the compounds that Mohammad has U and N values for (branched alkanes and alkynes) and which have good experimental data

3. We estimate Potoff generalized and NERD VLE from TraPPE simulations, Potoff S/L from Potoff generalized, and TraPPE from Potoff generalized
4. For $\lambda_{\text{ref}} = 12$ and $\lambda_{\text{rr}} = 16$, MBAR-GCMC predicts vapor density, vapor pressure, and heat of vaporization more accurately than liquid density
5. For $\lambda_{\text{ref}} = 12$ and $\lambda_{\text{rr}} = 12$, i.e., computing NERD from TraPPE simulations, MBAR-GCMC predicts all four properties accurately
6. We present how basis functions allow for rapid computation of wide range of parameter sets:
 - (a) *n*-hexane
 - (b) 2-methylpropane
 - (c) 2,2-dimethylpropane
 - (d) cyclopentane or cyclohexane
7. We provide supporting information with basis functions for several branched alkanes with TraPPE and Potoff force fields

3.1 Figures

1. Percent deviation between MBAR and HR results for ρ_{holiq} , ρ_{hovap} , P_{sat} , and ΔH_v
2. Comparison between MBAR bootstrapping and analytical uncertainties and HR uncertainties
3. Scaling of epsilon post-simulation for branched alkanes and alkynes
4. Prediction of VLE for $\lambda_{\text{ref}} \neq \lambda_{\text{rr}}$
5. Prediction of VLE for $\lambda_{\text{ref}} = \lambda_{\text{rr}} = 12$

6. Prediction of VLE for $\lambda_{\text{ref}} = \lambda_{\text{rr}} = 16$
7. Two-D scans of scoring functions for $\epsilon - \sigma$ of CH3 (a) and CH2 (b) for *n*-hexane
8. Two-D scans of scoring functions for $\epsilon - \sigma$ of CH3 (a) and CH (b) for 2-methylpropane
9. Two-D scans of scoring functions for $\epsilon - \sigma$ of CH3 (a) and C (b) for 2,2-dimethylpropane
10. Two-D scans of scoring functions for $\epsilon - \sigma$ of CH2 for cyclopentane or cyclohexane (reference is TraPPE)

4 Discussion/Limitations/Future work

As ITIC is more reliable at near-triple-point conditions, MBAR-ITIC and MBAR-GCMC can be combined to cover most temperatures that span the vapor-liquid coexistence curve.

1. We recommend that future GCMC-VLE studies report the snapshots of N and U and/or basis functions to recompute U as this allows for future force field optimization
2. Improvements are possible with multiple θ or simulating a range of μ values

5 Conclusions

6 Acknowledgments

Mostafa and J. Richard Elliott provided valuable insights.

References

- (1) Martin, M. G.; Siepmann, J. I. Transferable potentials for phase equilibria. 1. United-atom description of n-alkanes. *J. Phys. Chem. B* **1998**, *102*, 2569–2577.
- (2) Hemmen, A.; Gross, J. Transferable Anisotropic United-Atom Force Field Based on the Mie Potential for Phase Equilibrium Calculations: n-Alkanes and n-Olefins. *J. Phys. Chem. B* **2015**, *119*, 11695–11707.
- (3) Potoff, J. J.; Bernard-Brunel, D. A. Mie Potentials for Phase Equilibria Calculations: Applications to Alkanes and Perfluoroalkanes. *J. Phys. Chem. B* **2009**, *113*, 14725–14731.
- (4) Wick, C. D.; Siepmann, J. I. Self-adapting fixed-end-point configurational-bias Monte Carlo method for the regrowth of interior segments of chain molecules with strong intramolecular interactions. *Macromolecules* **2000**, *33*, 7207–7218.
- (5) Paluch, A. S.; Shen, V. K.; Errington, J. R. Comparing the Use of Gibbs Ensemble and Grand-Canonical Transition-Matrix Monte Carlo Methods to Determine Phase Equilibria. *Ind. Eng. Chem. Res.* **2008**, *47*, 4533–4541.
- (6) Hemmen, A.; Panagiotopoulos, A. Z.; Gross, J. Grand Canonical Monte Carlo Simulations Guided by an Analytic Equation of State-Transferable Anisotropic Mie Potentials for Ethers. *J. Phys. Chem. B* **2015**, *119*, 7087–7099.
- (7) McDonald, I. R.; Singer, K. Machine Calculation of Thermodynamic Properties of a Simple Fluid at Supercritical Temperatures. *The Journal of Chemical Physics* **1967**, *47*, 4766–4772.
- (8) Card, D. N.; Valleau, J. P. Monte Carlo Study of the Thermodynamics of Electrolyte Solutions. *The Journal of Chemical Physics* **1970**, *52*, 6232–6240.

- (9) Wood, W. W. Monte Carlo Calculations for Hard Disks in the Isothermal–Isobaric Ensemble. *The Journal of Chemical Physics* **1968**, *48*, 415–434.
- (10) Panagiotopoulos, A. Z. Monte Carlo methods for phase equilibria of fluids. *Journal of Physics: Condensed Matter* **2000**, *12*, R25.
- (11) Chodera, J. D.; Swope, W. C.; Pitera, J. W.; Seok, C.; Dill, K. A. Use of the weighted histogram analysis method for the analysis of simulated and parallel tempering simulations. *J. Chem. Theory Comput.* **2007**, *3*, 26–41.
- (12) Shirts, M. R.; Chodera, J. D. Statistically optimal analysis of samples from multiple equilibrium states. *J. Chem. Phys.* **2008**, *129*, 124105.
- (13) Boulougouris, G. C.; Peristeras, L. D.; Economou, I. G.; Theodorou, D. N. Predicting fluid phase equilibrium via histogram reweighting with Gibbs ensemble Monte Carlo simulations. *The Journal of Supercritical Fluids* **2010**, *55*, 503 – 509, 100th year Anniversary of van der Waals’ Nobel Lecture.
- (14) Messerly, R. A.; Razavi, S. M.; Shirts, M. R. Configuration-Sampling-Based Surrogate Models for Rapid Parameterization of Non-Bonded Interactions. *Journal of Chemical Theory and Computation* **2018**, *14*, 3144–3162.
- (15) Messerly, R. A.; Shirts, M. R.; Kazakov, A. F. Uncertainty quantification confirms unreliable extrapolation toward high pressures for united-atom Mie λ -6 force field. *The Journal of Chemical Physics* **2018**, *149*, 114109.
- (16) Razavi, S. M. Optimization of a Transferable Shifted Force Field for Interfaces and Inhomogeneous Fluids using Thermodynamic Integration. M.Sc. thesis, The University of Akron, 2016.

- (17) Razavi, S. M.; Messerly, R. A.; Elliott, J. R. Coexistence Calculation Using the Isothermal-Isochoric Integration Method. **2018**, *Pending publication*.
- (18) Errington, J. R.; Panagiotopoulos, A. Z. Phase equilibria of the modified Buckingham exponential-6 potential from Hamiltonian scaling grand canonical Monte Carlo. *The Journal of Chemical Physics* **1998**, *109*, 1093–1100.
- (19) Errington, J. R.; Panagiotopoulos, A. Z. A new intermolecular potential model for the n-alkane homologous series. *J. Phys. Chem. B* **1999**, *103*, 6314–6322.
- (20) Errington, J. R.; Panagiotopoulos, A. Z. New intermolecular potential models for benzene and cyclohexane. *The Journal of Chemical Physics* **1999**, *111*, 9731–9738.
- (21) Weidler, D.; Gross, J. Individualized force fields for alkanes, olefins, ethers and ketones based on the transferable anisotropic Mie potential. *Fluid Phase Equilibria* **2018**,
- (22) Martin, M. G.; Siepmann, J. I. Novel Configurational-Bias Monte Carlo Method for Branched Molecules. Transferable Potentials for Phase Equilibria. 2. United-Atom Description of Branched Alkanes. *The Journal of Physical Chemistry B* **1999**, *103*, 4508–4517.
- (23) Shah, M. S.; Siepmann, J. I.; Tsapatsis, M. Transferable potentials for phase equilibria. Improved united-atom description of ethane and ethylene. *AIChE J.* **2017**, *63*, 5098–5110.
- (24) Mick, J. R.; Soroush Barhaghi, M.; Jackman, B.; Schwiebert, L.; Potoff, J. J. Optimized Mie Potentials for Phase Equilibria: Application to Branched Alkanes. *J. Chem. Eng. Data* **2017**, *62*, 1806–1818.
- (25) Nath, S. K.; Escobedo, F. A.; de Pablo, J. J. On the simulation of vapor-liquid equilibria for alkanes. *J. Chem. Phys.* **1998**, *108*, 9905–9911.

- (26) Allen, M. P.; Tildesley, D. J. *Computer simulation of liquids*; Clarendon Press ; Oxford University Press: Oxford England New York, 1987; pp xix, 385 p.
- (27) Barhaghi, M. S.; Mick, J. R.; Potoff, J. J. Optimised Mie potentials for phase equilibria: application to alkynes. *Molecular Physics* **2017**, *115*, 1378–1388.
- (28) Naden, L. N.; Shirts, M. R. Rapid Computation of Thermodynamic Properties Over Multidimensional Nonbonded Parameter Spaces using Adaptive Multistate Reweighting. *J. Chem. Theory Comput.* **2016**, *12*, 1806–1823.
- (29) Dybeck, E. C.; König, G.; Brooks, B. R.; Shirts, M. R. Comparison of Methods To Reweight from Classical Molecular Simulations to QM/MM Potentials. *J. Chem. Theory Comput.* **2016**, *12*, 1466–1480.

7 Supporting Information

7.1 MBAR VLE estimates

Provide tables of MBAR estimates

7.2 Basis functions

1. Validation that basis functions give accurate energies

7.3 Raw data

1. Comparison of 2-D histograms for TraPPE and Potoff. MBAR overlap, possible?
Probably not without rerunning the simulations.